PERGAMON

Journal of Structural Geology 25 (2003) 183–196

JOURNAL OF STRUCTURAL GEOLOGY

www.elsevier.com/locate/jsg

Dilational normal faults

David A. Ferrill[a,*], Alan P. Morris[b]

[a]CNWRA, Southwest Research Institute, 6220 Culebra Road, San Antonio, TX 78238, USA
[b]Department of Earth and Environmental Science, University of Texas at San Antonio, San Antonio, TX 78249, USA

Received 8 July 2001; accepted 6 February 2002

Abstract

At low differential effective stress and with minimum principal effective stress near zero or tensile, rocks fail in several modes and with variable failure angles. Under these conditions mechanical stratigraphy exerts a significant influence on initial dip of normal faults. Less competent layers fail in shear mode along fractures that approximate the failure angle predicted by a standard rock mechanics analysis. Deformation of more competent layers, which is driven in part by interaction with the more rapidly deforming incompetent layers, produces hybrid mode failure in which failure angles are smaller than in shear mode. Analyses of small-displacement (<1 m displacement) normal faults cutting Cretaceous carbonate strata in west Texas (USA) indicate that fault geometries resulting from this effect commonly display steep segments where the fault traverses more competent beds. Displacement on these faults has caused dilation of steeper segments. Analogous steep dilational fault segments host ore deposits in the North Pennine Orefield, England. Dilatant segments along faults within carbonates of the Cretaceous age Edwards Group near San Antonio, Texas (USA) have been enlarged by groundwater flow, and are important permeability and shallow groundwater infiltration pathways.

Keywords: Normal faults; Effective stress; Failure angles

1. Introduction

Normal faults in stratified rocks commonly have dip changes that are visible in dip-parallel profiles. Variation in normal fault dip can be caused by various mechanisms, including; (i) differential compaction of sedimentary layers after fault formation (Xiao and Suppe, 1989); (ii) active fault deformation (e.g. by slip or shear along layering or intersecting faults; Ferrill et al., 1998, 2000); (iii) linkage of an originally vertically-segmented fault (Peacock and Zhang, 1994; Childs et al., 1996; Mansfield and Cartwright, 1996); and (iv) fault initiation with failure angles controlled by rock mechanical properties and effective stresses at the time of failure (Mandl, 1988; Peacock and Sanderson, 1992).

We describe exposure-scale normal faults in Cretaceous carbonate strata in west Texas, where characteristic fault dips are associated with particular lithologic units. These faults lack the diagnostic traits of passive deformation (differential compaction) or active deformation (e.g. slip or shear along layering), or of development from originally vertically segmented faults (e.g. abandoned fault tips or splays). We interpret the dip changes to be primary features of the faults, developed during fault nucleation and growth, and controlled by the failure mode and failure angle of the mechanical layers experiencing the faulting. Similar dilational normal faults are sites for mineralization in the North Pennine Orefield, and also may be important sources of porosity and permeability in hydrocarbon reservoirs. We use examples of faults with dip changes in Edwards Aquifer strata in south-central Texas to illustrate the importance of dilation on steep fault segments to groundwater infiltration and flow.

2. Background

The angle of shear failure (θ, measured between the maximum principal compressive stress and the failure plane) in rock can be predicted from the angle of internal friction (friction angle, φ) using the following equation (Mandl, 1988):

$$\theta = \pm(45^\circ - \varphi/2) \quad (1)$$

Failure mode depends upon the differential stress [difference between maximum principal compressive stress (σ_1) and minimum principal compressive stress (σ_3)] the effective minimum principal compressive stress (σ'_3;

* Corresponding author. Fax: +1-210-522-5155.
E-mail address: dferrill@swri.edu (D.A. Ferrill).

0191-8141/02/$ - see front matter
PII: S0191-8141(02)00029-9

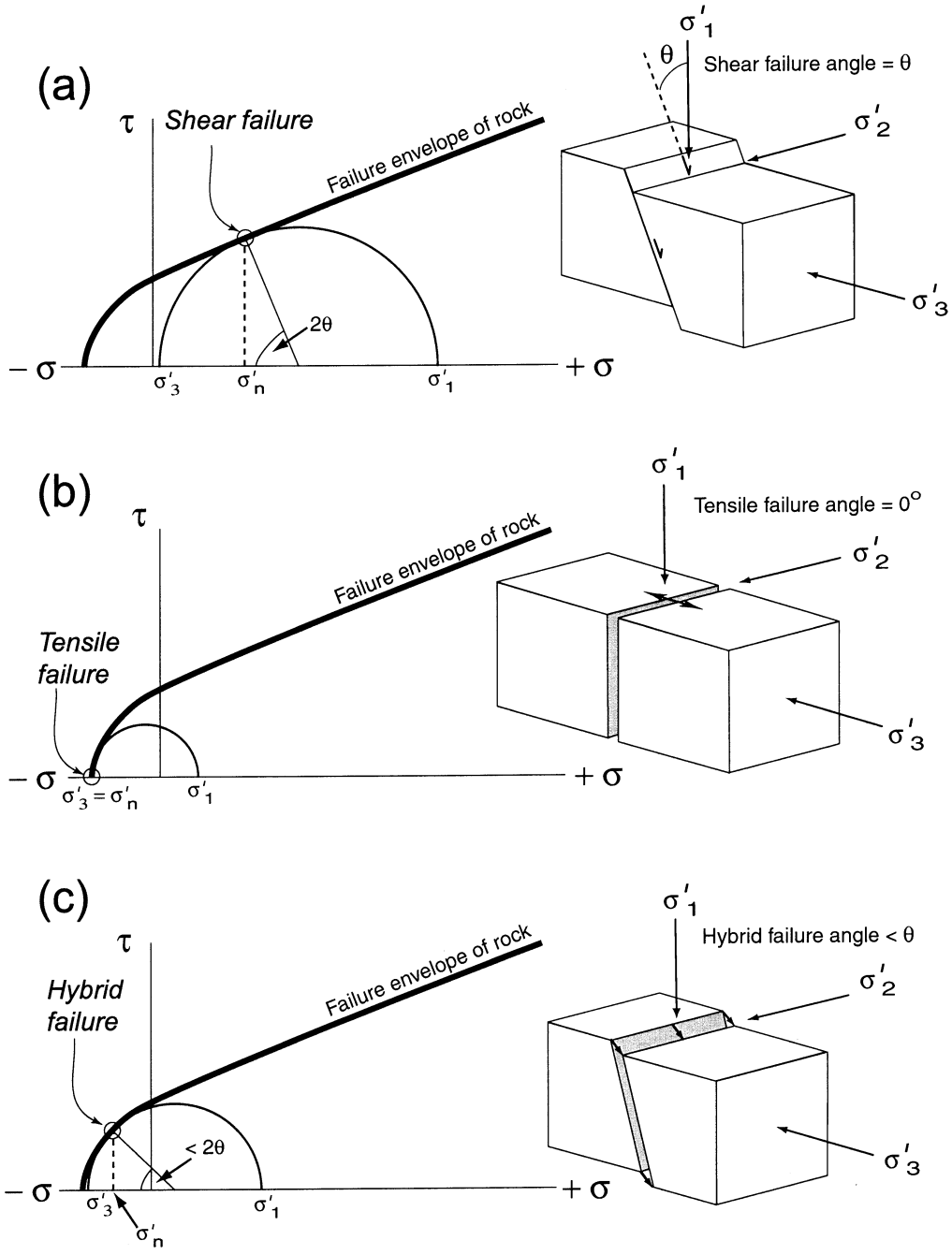

Fig. 1. Mohr-space diagrams with Hoek–Brown failure envelope (1988) illustrating different failure modes: (a) shear failure, (b) tensile failure, (c) hybrid failure.

$\sigma'_3 = \sigma_3 - P_f$, where P_f = pore fluid pressure) at the time of failure, and upon the strength characteristics of the rock (Fig. 1). There are three general possibilities (Hancock, 1985; Mandl, 1988):

1. Shear failure, in which displacement is parallel to the fracture surface, and the effective normal stress (σ'_n) acting on the fracture surface, $\sigma'_3 < \sigma'_n \geq 0$. The failure angle for this mode is given by Eq. (1) (Fig. 1a).
2. Tensile failure in which displacement is perpendicular to the fracture surface. In this case $\sigma'_3 = \sigma'_n < 0$ and $|\sigma'_3| \geq$ tensile strength of the rock. The failure angle for this mode is 0° (Fig. 1b).
3. Hybrid failure, in which displacement is oblique to the fracture surface ('dilatant faults'; Mandl, 1988). In this case $\sigma'_3 < \sigma'_n < 0$ and $|\sigma'_3| <$ tensile strength of the rock. The failure angle for this mode lies between 0° and the angle predicted by Eq. (1) (Fig. 1c).

3. Analysis of natural examples from west Texas, USA

Horizontal to gently dipping layers of the Cretaceous Buda Limestone (Barnes, 1976; Anderson et al., 1995) exposed along Interstate Highway 10 (I-10), in west Texas are cut by normal faults with displacements of less than 1 m. At a roadcut exposure along eastbound I-10 at mile marker 195 (approximately 16 km west of Balmorhea, Texas), several faults have consistent dip changes through the various limestone layers (Fig. 2a). Layers in the exposure dip gently, between horizontal and 10°. The faults described here are associated with changes in layer dip of a few degrees.

3.1. Fault shapes

Faults are undulatory, cutting layering at 80–90° in layers K and H (Fig. 2b–e; Table 1), and generally 65–75° in other layers. Fault dip changes tend to be gradual rather than abrupt (Fig. 2a–e). Normal offset is approximately parallel to more shallowly dipping fault segments, and causes dilation at steep fault segments. Dilational fault segments of this sort have been referred to as dilational jogs (Sibson, 1996), or releasing bends (Groshong, 1988). In one case, a dissolution cavity has formed (Fig. 2b), indicating localized groundwater flow along the dilational fault segment.

3.2. Fault zones

Fault zone materials consist of a combination of crystalline calcite veins, rock fragments, and clay sized material (Fig. 3a). Along the walls of the dilatant steep segment, veins of milky calcite (up to 50 mm thick) are locally present (Fig. 3b). Calcite crystals in these veins range from 5 to 15 mm across, and in some cases have euhedral terminations toward the vein centers. Along slip surfaces, coarse calcite veins that are well bonded with the wall rock are common. These veins are typically 2–5 mm thick, and consist of equant to elongate crystals 2–5 mm across. The central part of the fault zones generally consists of angular to rounded carbonate rock fragments (1–30 mm diameter) and clayey (some iron rich) material (Fig. 3b). The filling tends to be amorphous, especially in dilational fault segments, but in some cases the fill is layered parallel to the walls along fault segments that parallel the slip direction. Tan colored, fine grained calcite veneer is common on wall rock interfaces and on open fracture surfaces within the fault zone. This finely crystalline material has the appearance of flowstone and suggests precipitation along open cavity walls under unsaturated conditions.

3.3. Interpretation

We interpret the fault zone material to be a combination of crushed wall rock, sediment washed into dilational segments, and precipitated calcite. Based on lack of similarity between the composition of this fault zone material and the host rock, and presence of rounded rock fragments, we interpret this material to have been transported in, probably by lateral groundwater flow along the fault.

Failure angles for rocks undergoing shear tend to be on the order of 10–20° for competent rocks, and 15–45° for less competent rocks (Mandl, 1988). These angles decrease to 0° for hybrid to tensile failure modes (Fig. 1). If we assume that faulting initiated when layering was horizontal, then the angles between the faults and bedding represent the initial fault dips and the failure angle for each fault segment is 90° minus fault segment dip (Table 1). The faults investigated failed at a range of angles from 1 to 40°, and individual layers have consistent failure angles (Table 1). The lowest failure angles are comparable with those of competent rock failing in the hybrid mode, and generate a dilational sense of displacement (see layers K and H in Figs. 2b–e and 3a and b). Net slip on the faults was parallel to the sections with shallower dips, and consequently, the steeper fault sections dilated.

3.4. Origin of fault dip variation

Peacock and Zhang (1994) interpreted faults that are refracted through mechanical stratigraphy to have initiated as extension fractures in brittle layers (limestone), then propagated upwards and downwards into ductile layers (shale). Resulting dilational fault segments [referred to as 'pull-aparts' or 'extensional bends' by Peacock and Zhang (1994)] were filled by calcite or mud rock material that flowed in from adjacent shale beds [figure 4a in Peacock and Zhang (1994)]. In contrast, the rock sequence we analyzed appears to have been brittle under the deformation conditions at the time of faulting.

We interpret the variations in dip of faults we investigated in west Texas to be the result of variations in the mechanical strength of rock layers coupled with low values of effective stress and a minimum principal effective stress (σ'_3) that is weakly compressive to tensile (Fig. 4). These conditions can cause different layers to fail in different modes, hence generating markedly different fracture orientations from bed to bed. In our interpretation, those beds that exhibit steeper fault dips are more competent under the conditions during defaulting than those with shallower fault dips.

Two broad possibilities exist with respect to relative timing of failure in a mechanical multilayer. Failure may nucleate first in either the stronger (e.g. Peacock and Zhang, 1994) or weaker layers (e.g. Wilkins and Gross, 2002) depending on the strength and relative proportions of the mechanical layers and the effective stresses (especially differential stress) experienced by the mechanical layers. In the normal faulting regime, maximum principal compressive stress (σ_1) is vertical, and is controlled by ρgh (density × gravity × depth). The vertical effective stress ($\sigma'_1 = \sigma_1 - P_f$) increases downward primarily as a function of depth. Therefore σ'_1 in both strong and weak layers at a

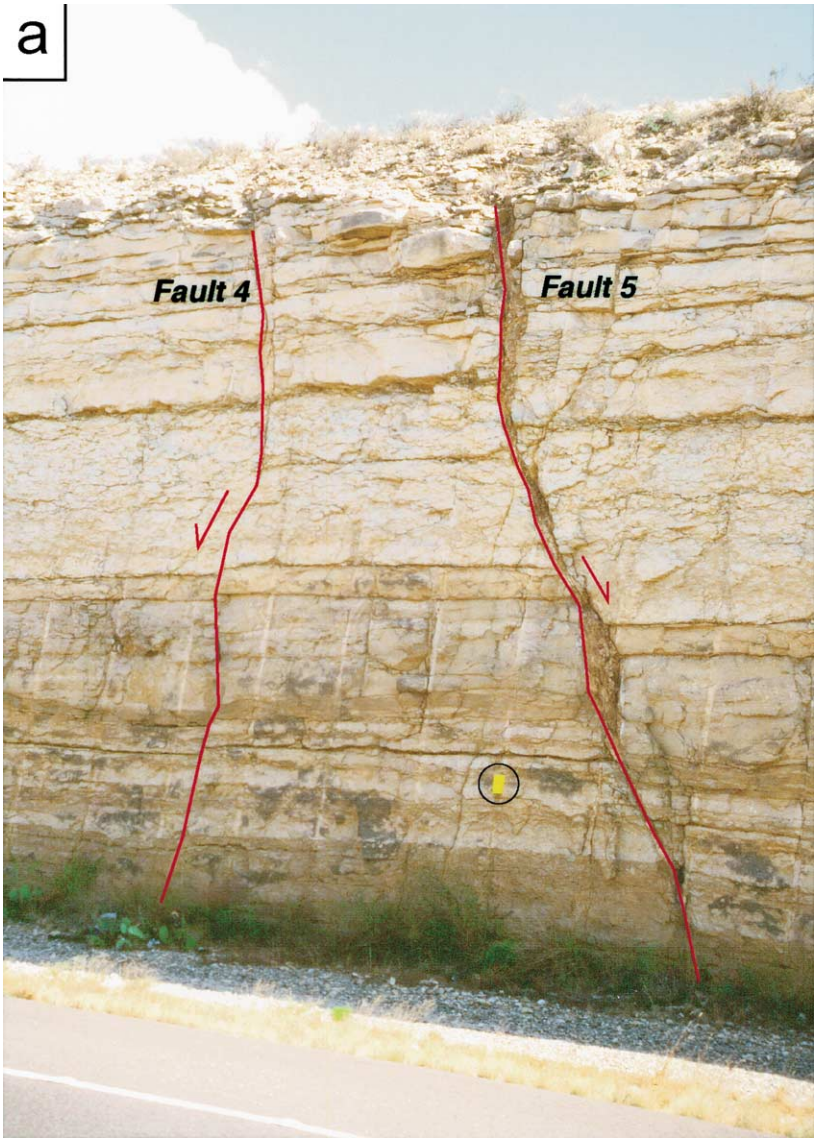

Fig. 2. Photographs showing normal faults cutting limestone layers in the Buda Limestone, along I-10 East near Balmorhea, Texas. Field Notebook, 12 cm × 9 cm for scale. (a) Horst between northeast-dipping fault (4) and southwest-dipping fault (5). (b) Northeast-dipping horst-bounding fault (4) has 9 cm displacement. (c) Southwest-dipping horst-bounding fault (5) has 77 cm displacement. Note dilatant steep segments and that horizontal dilation across these segments equals heave component of fault slip. (d) Northeast-dipping fault (8) has 7 cm displacement near the base of the exposure, and loses displacement upward to a tip in layer J. (e) Southwest-dipping fault (10) has 15 cm displacement near the base of the exposure, and loses displacement upward to a tip in layer J.

point on a mechanical layer interface would be essentially the same. Horizontal σ'_3 magnitude may fluctuate with depth, as a function of the ability of different mechanical layers to support the differential stress. A strong layer such as limestone can support a larger differential stress than a weak layer like shale. Thus, strong layers in a multilayer may behave as reinforcing beams, in which case differential stress varies layer by layer prior to failure. In this case of strong layer reinforcement, hybrid failure would occur in the strong layer first (stress state B in Fig. 4). Once the fracture propagates to the weak layer, the weak layer will no longer be reinforced by the strong layer and the magnitude of σ'_3 experienced by the weak layer will be decreased, increasing the differential stress and causing shear failure in the weak layer (stress state A in Fig. 4).

In the case where the stress state within a weaker layer produces initial shear failure (stress state A, Fig. 4), traction between the deforming weaker layer and the as yet intact stronger layer causes stress magnification and concentration in the stronger layer. Because the stronger layer will not fail at the same differential stress level as the weaker layer, the differential stress increases as σ'_3 decreases (becomes increasingly tensile). The vertical σ'_1 is unchanged because

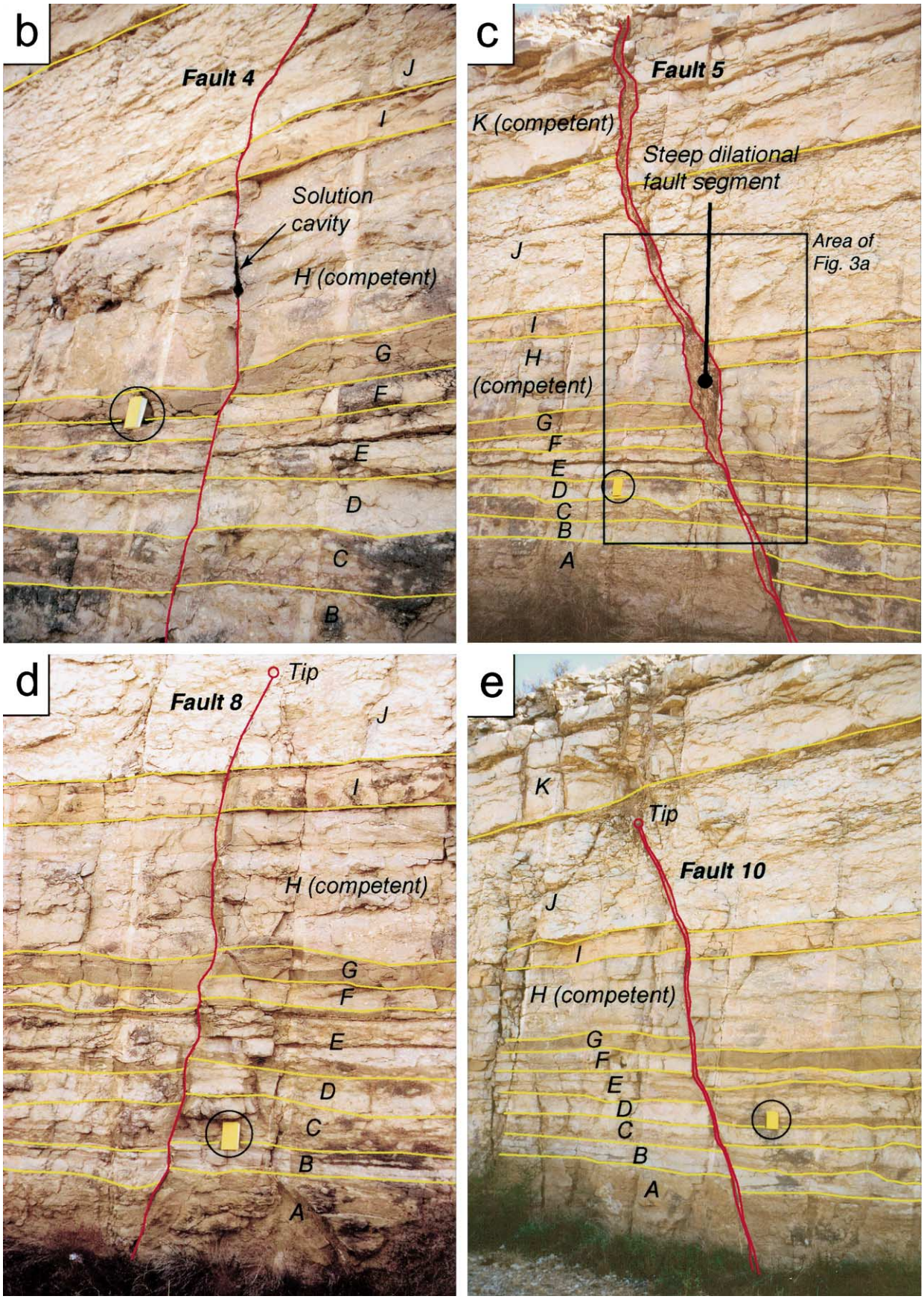

Fig. 2. (*continued*)

Table 1
Fault segment and bedding orientation data for faults in the Balmorhea exposure. Failure angle is calculated assuming that faulting initiated when strata were horizontal. Unit subdivisions are based on lithologic properties and fault-bedding intersection angles. Bedding orientation is 318/05 adjacent to faults 4, 8, and 10. Bedding orientation is 318/04 adjacent to fault 5. Balmorhea exposure is along I-10 in west Texas near (UTM zone 13; NAD 27) 601498 m E, 3434845 m N, and 1105 m elevation

	Fault strike	Fault dip	Corrected fault strike	Corrected fault dip	Failure angle
Fault 4					
K (competent)	149	82	149	87	3
J	329	70	329	65	25
I	327	83	327	78	12
H (competent)	148	83	148	88	2
G	330	71	330	66	24
F	329	83	329	78	12
E	329	83	329	78	12
D	327	79	327	74	16
C	327	79	327	74	16
B	327	79	327	74	16
A	327	79	327	74	16
Fault 5					
K (competent)	149	90	329	86	4
J	149	72	149	76	14
I	149	72	149	76	14
H (competent)	149	85	149	89	1
G	161	64	161	68	22
F	161	64	161	68	22
E	161	64	161	68	22
D	161	64	161	68	22
C	179	70	179	74	16
B	179	70	179	74	16
A	168	62	168	66	24
Fault 8					
K	Above tip				
J	328	65	328	60	30
I	328	79	328	74	16
H (competent)	328	86	328	81	9
G	328	65	328	60	30
F	148	86	328	89	1
E	328	65	328	60	30
D	148	88	328	87	3
C	328	64	328	59	31
B	328	81	328	76	14
A	328	76	328	71	19
Fault 10					
K	Above tip				
J	145	87	325	88	2
I	145	56	145	61	29
H (competent)	145	84	145	89	1
G	145	84	145	89	1
F	155	46	155	51	39
E	155	46	155	51	39
D	155	46	155	51	39
C	152	63	152	68	22
B	155	75	155	80	10
A	155	75	155	80	10
Averages					Bed thickness (cm)
	Lithologies				
K (competent)	Bedded to moderately massive fossiliferous packstone/wackestone			86.5	3.5
J	Fossiliferous wackestone, wavy to sutured stylolites common, shaley base			72.25	17.75
I	Calcareous sandstone			72.25	17.75
H (competent)	Massive, highly fossiliferous, poorly sorted, spar cemented grainstone			86.75	3.25
G	Buff wackestone/packstone			70.75	19.25
F	Gray packstone/wackestone			71.5	18.5
E	Buff colored wackestone/packstone			64.25	25.75
D	Gray packstone/grainstone			70	20
C	Buff colored wackestone/packstone			68.75	21.25
B	Gray packstone/grainstone			76	14
A	Buff colored wackestone/packstone			72.75	17.25

it is a function of the overlying rock. Ultimately, deformation of the weaker layer generates a large enough differential stress for the stronger layer to fail in hybrid mode (stress state B, Fig. 4).

A consequence of failure occurring under different conditions in the two mechanical layers is that the failure angle in each layer is different. Specifically, the failure angle in the stronger layer is smaller than that in the weaker layer, which produces steep fault segments in the stronger layer and more gentle fault dips in the weaker layer (Fig. 4). This can be thought of as refraction of the fault trajectory as the fracture propagates through the rock mass. The direction of propagation (from strong layers to weak layers, or from weak layers to strong layers; vertically or horizontally) does not affect these failure angles. In general, the optimal (that requiring least energy to generate) fracture trajectory will be shorter in stronger layers than in weaker layers.

The stress conditions illustrated in Fig. 4 are those for unsaturated carbonate rocks at depths of about 250–300 m. A similar situation could arise in saturated conditions where the pore fluid pressure is sufficiently elevated to generate a tensile σ'_3, and differential effective stress is low enough to straddle the shear failure/hybrid failure transition. Fault dip variation can also occur without failure mode switching resulting from differences in friction angle (see Eq. (1)). However, when, as in this case, steeper fault segment dips exceed typical dips for shear failure, mode switching is a likely mechanism.

3.5. Slip tendency analysis

An alternative perspective on tendency for fault-parallel sliding versus fault segment dilation is provided by an analysis of resolved shear- and normal-stress components. Slip tendency is the ratio of resolved shear stress to resolved normal stress on a surface (Morris et al., 1996). At the time of sliding, slip tendency equals the frictional resistance to sliding on a fault surface. Thus far, our analysis has focused on the conditions influencing fault initiation. Once a fault has formed, however, the locus and direction of slip are controlled by the confining pressure, the resolved stresses and resulting slip tendency, and the frictional resistance to sliding for each fault segment. The thicknesses and distributions of layers with different mechanical properties—the mechanical stratigraphy—are expected to exert a critical influence on slip direction. Mechanical properties of layers influence failure angles and fault dip, and thicknesses influence the height of dip segments.

Slip tendency analysis of faults from the Balmorhea exposure described here yields the results illustrated in Fig. 5. The σ_3 direction is approximately ENE–WSW (070°), which corresponds to the extension experienced by west Texas as the southern Basin and Range and Rio Grande Rift developed during the late Tertiary (Zoback et al., 1981). In this analysis, we assume a simple Andersonian normal faulting regime, with the magnitude of the intermediate principal compressive stress centered between the maximum and minimum compressive stress magnitudes. The steeper faults shown in profile as blue lines have low resolved normal stress and low resolved shear stress, and, therefore, they are in low slip tendency orientations. These steep fault segments, approximately perpendicular to σ_3, have a very high dilation tendency (Ferrill et al., 1999). High dilation tendency segments tend to dilate in response to the same stress field that produces slip on the less steep (ideally oriented) fault segments.

4. Significance for ore mineralization

The dilational faulting in the Balmorhea exposure bears a very strong resemblance to 'fissure veins' that have been mined from the North Pennine Orefield in England for almost 2000 years (Wallace, 1861; Dunham, 1988). Wallace (1861) and Dunham (1988) recognized and described the relationship between dip of mineralized vein fractures and the physical properties of the associated (primarily Carboniferous age) wall rock, observing that steep fault segments occur in sandstone and limestone layers, and more gentle fault segments occur in shale and thin coal beds. Normal displacements of 1–10 m on faults produced dilation where fault segments are steep, and little or no dilation where fault dips are more gentle. Wallace (1861) illustrated an idealized ore vein occupying a fault refracted through the stratigraphic sequence (Fig. 6a). Ore-filled dilational fault segments are associated with each limestone or sandstone layer, and are separated by very thin veins associated with shale layers and coal seams. The dilational fault segments are referred to as 'ribbon oreshoots' whose dimensions are vertically limited by thickness of the host sandstone or limestone layers, but are laterally extensive. Dunham (1988) noted that fluid movement would have been dictated by 'ribbon-like openings' along dilational fault segments, which provided pathways for lateral fluid movement. Fluid channels in limestones are thought to have been locally enhanced by dissolution where flow was concentrated beneath a weak and impermeable bed (Dunham, 1988). Mineral variation is most obvious along fault strike, further supporting the lateral nature of fault-related flow pathways.

A major emphasis of Dunham's (1988) paper is that ore mineralization appears to be depth limited. The greatest depth of mining in the Pennines is 400 m, and few workings extend below 200 m depth. To partially explain this phenomenon, Dunham (1948) suggested that bending related to dome formation caused greater fault dilation at shallow depths, and progressively less dilation downwards (Fig. 6b). This is an outer arc extension model. Consequently, mineralized dilational fault segments progressively pinch out with depth as a function of radius of curvature of the dome and position of the neutral surface. Our model provides an alternative explanation for depth-restricted mineralization of dilational normal faults. Fault refraction resulting from contrasting failure modes in adjacent

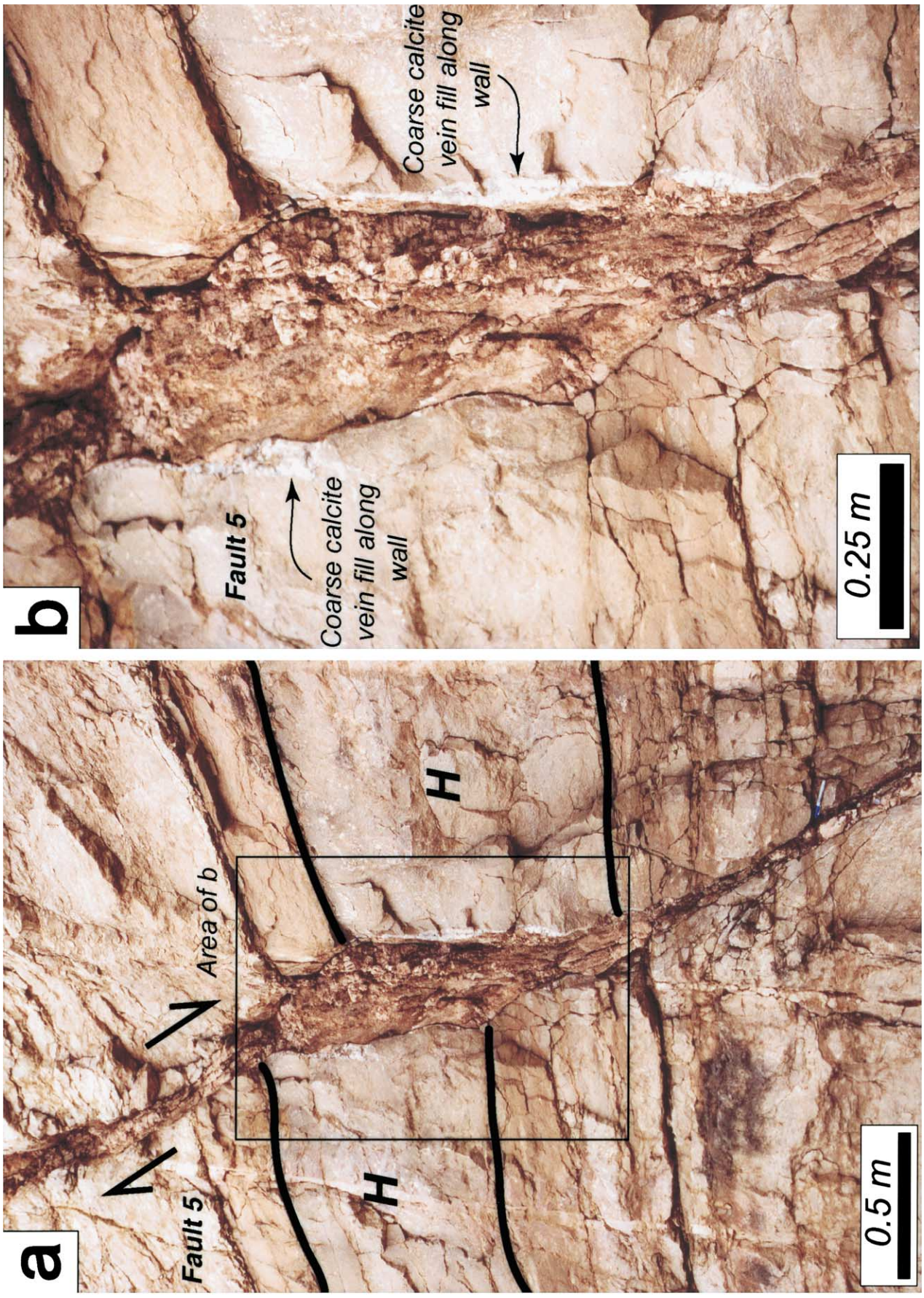
a
Fault 5
Area of b
H
H
0.5 m
b
Fault 5
Coarse calcite vein fill along wall
Coarse calcite vein fill along wall
0.25 m

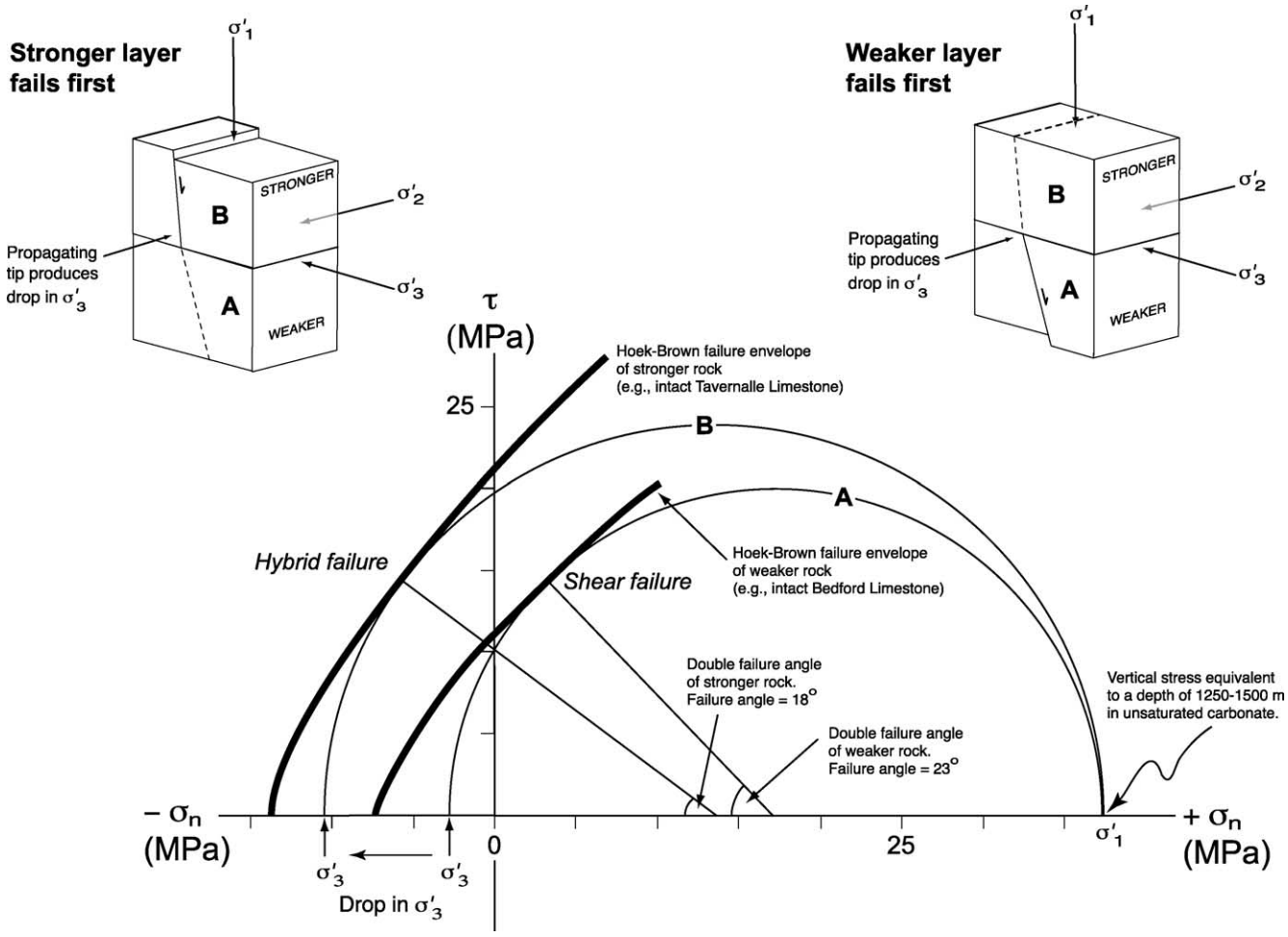

Fig. 4. Mohr-space diagram illustrating how contrasting mechanical stratigraphy leads to different failure mode and failure angles in different layers. A more competent rock (e.g. Tavernalle Limestone) is more likely to fail in hybrid mode than a less competent rock (e.g. Bedford Limestone) under the same normal faulting stress regime. See text for details. Equation and rock-quality parameters for generating failure envelopes from Hoek and Brown (1988) rock strength data from table 3.1 in Goodman (1980).

mechanical layers requires low differential stress, otherwise tensile or hybrid failure would not occur. In areas of active normal faulting, differential stress increases with depth and low differential stress is limited to shallow depths (Engelder, 1993). Differential stresses corresponding to depths greater than about 1 km would produce shear failure rather than hybrid or tensile failure in most sedimentary rocks. Consequently, deeper than about 1 km, fault refraction is likely to be controlled by change in shear failure angle in adjacent layers, rather than contrasting failure mode. Fault refraction angles resulting from changes in shear failure angle tend to be smaller than dip changes associated with change in failure mode, therefore generate less dilation with fault slip.

5. Significance for faulted limestone aquifers

The Edwards Aquifer of south-central Texas is composed of Cretaceous limestones of the Edwards Group, which includes a lower part (the Kainer Formation) and an upper part (the Person Formation), and the overlying Georgetown Formation (Maclay and Small, 1983). These rocks crop out in the Edwards Plateau region, and their southern and eastern outcrop boundary is within the Balcones Fault system, a zone of Tertiary age, down to the southeast, normal faulting (Maclay and Small, 1983; Stein and Ozuna, 1996; Clark, 2000; Collins, 2000). South and east of the Balcones fault system, the Edwards Aquifer is confined beneath younger sedimentary rocks and serves as the primary water source

Fig. 3. Details of fault zone and dilational fault segment filling material along southwest dipping fault 5. See Fig. 2c for location of (a). Coarse white calcite vein fill along walls of dilational fault segment visible in (b) is present on both walls of the dilational fault segment and probably represents an earliest increment of fault slip and fault zone filling material.

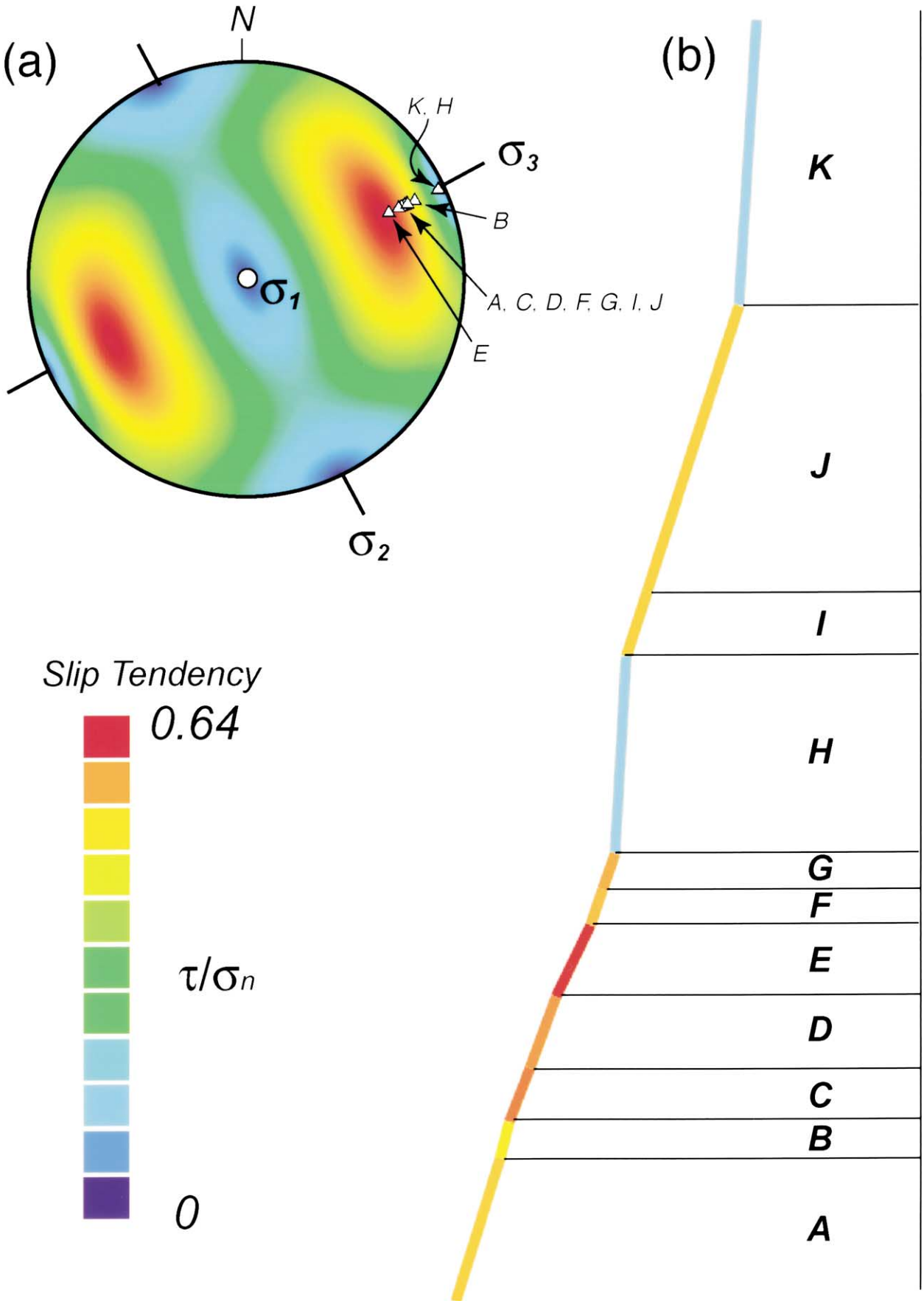
(a)
N
K, H
σ3
B
σ1
A, C, D, F, G, I, J
E
σ2
Slip Tendency
0.64
τ/σn
0
(b)
K
J
I
H
G
F
E
D
C
B
A

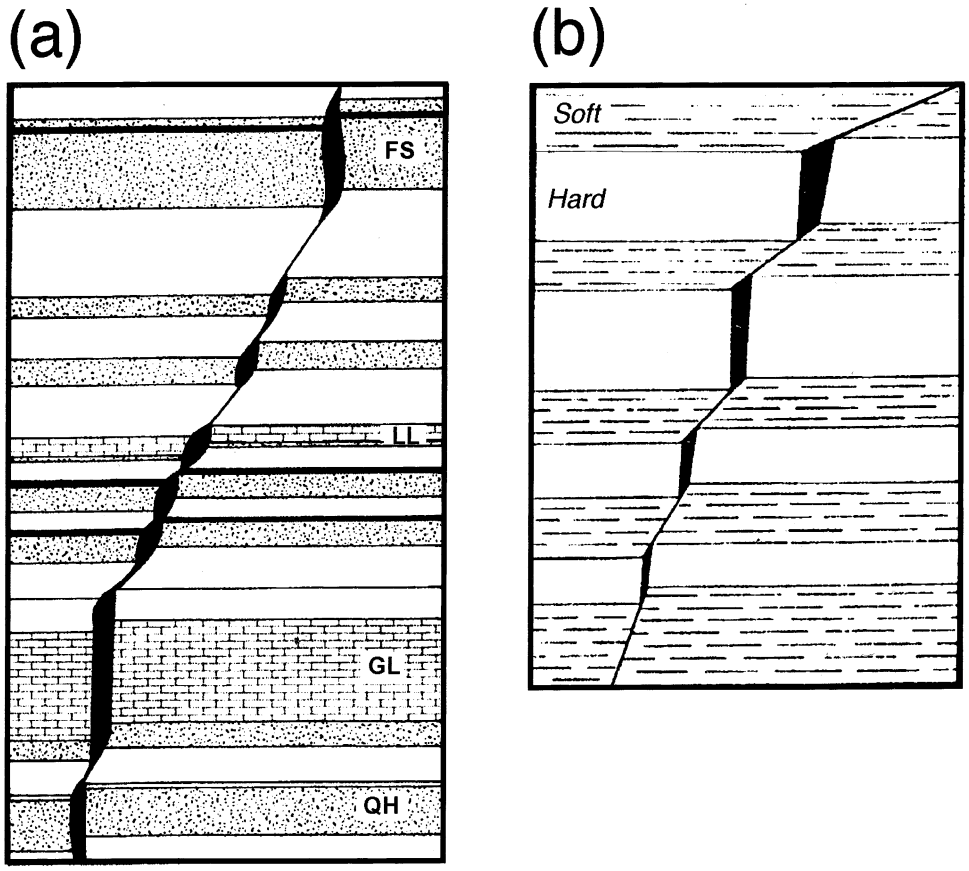

Fig. 6. Idealized vertical cross-sections through a Pennine fissure vein. (a) Illustration from Wallace (1861) showing ore vein (black) cutting limestone (brick pattern; LL = Little Limestone, GL = Great Limestone), sandstone (stipple pattern; FS = Firestone, QH = Quarry Hazle), shale (unpatterned), and coal (thin black layers). (b) Model from Dunham (1948) illustrating upward increasing dilation of an ore vein, occupying a dilational normal fault, interpreted to be the result of bending (outer arc extension) related to doming. 'Soft' refers to shale and coal layers, and 'hard' refers to limestone and sandstone layers. Reproduced with permission of the Yorkshire Geological Society, from Dunham (1988).

for many communities, including being the sole source of water for the city of San Antonio (Sharp and Banner, 1997; Hovorka et al., 1998). Most significant recharge for the aquifer occurs along the Balcones fault system where faults and fractures and dissolution-features such as sink holes and caves are considered to be major sites for groundwater recharge (Clark, 2000). By analogy with surface exposures, the high-volume, high flow-rate subsurface flow is also likely to be dominated by faults, fractures, and solution cavities (Hovorka et al., 1998).

Not all faults within the aquifer system are conduits for either flow or recharge, and not all segments of a single fault have the same hydraulic properties. Small-displacement (<1 m displacement) normal faults in the grainstone-rich upper section of the Kainer Formation, in the Balcones Fault system near San Antonio, exhibit dip changes at lithologic boundaries. These dip changes are similar to, but less dramatic than, the examples from west Texas (Fig. 7), probably owing to a lower competence contrast or higher differential stress than the example from the Balmorhea exposure in west Texas. The two examples shown in Fig. 7 display dissolution features that parallel fault-bedding intersections at mechanical layer boundaries. In one example (Fig. 7a), a cave is forming parallel to the steep fault segment, associated with an 18° change in fault dip. Other cavities at dip changes along the fault (within layer A in Fig. 7a) have been filled by calcite precipitation. The cave that parallels the fault-bedding intersection shown in Fig. 7b extends at least 10 m along the fault into the rock exposure. The fault trace is visible along the length of the cave ceiling. Open apertures along the fault, however, are generally small, on the order of 2 mm or less, indicating minor dilation of the

Fig. 5. Slip tendency analysis for average fault geometry based on faults illustrated in Figs. 2 and 3 (see averages in Table 1). $\sigma_2 = 65\%$ of σ_1; $\sigma_3 = 30\%$ of σ_1; σ_1 is vertical; σ_2 horizontal, azimuth 160°; σ_3 horizontal, azimuth 070°. (a) Slip tendency plot illustrates the pattern of slip tendency, and triangles represent poles (dip corrected) to average fault orientations for each bed illustrated in Fig. 2 and tabulated in Table 1. (b) Cross-sectional profile of fault geometry color coded according to slip tendency in interpreted stress field at the time of faulting, as shown in (a). Analysis performed using 3DStress™ v. 1.3.3.

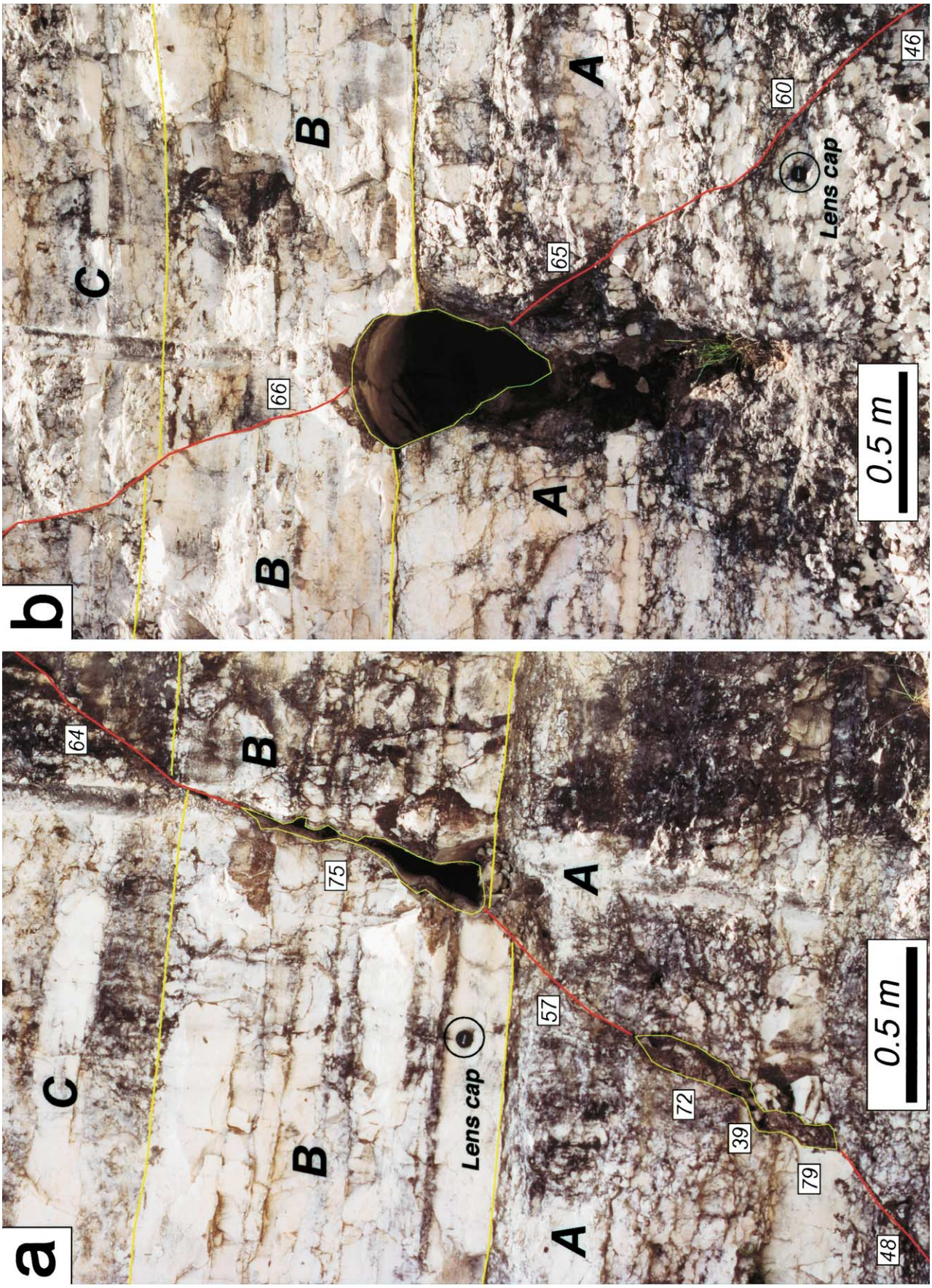
a
b
C
B
A
64
75
57
72
39
79
48
Lens cap
0.5 m
66
65
60
46

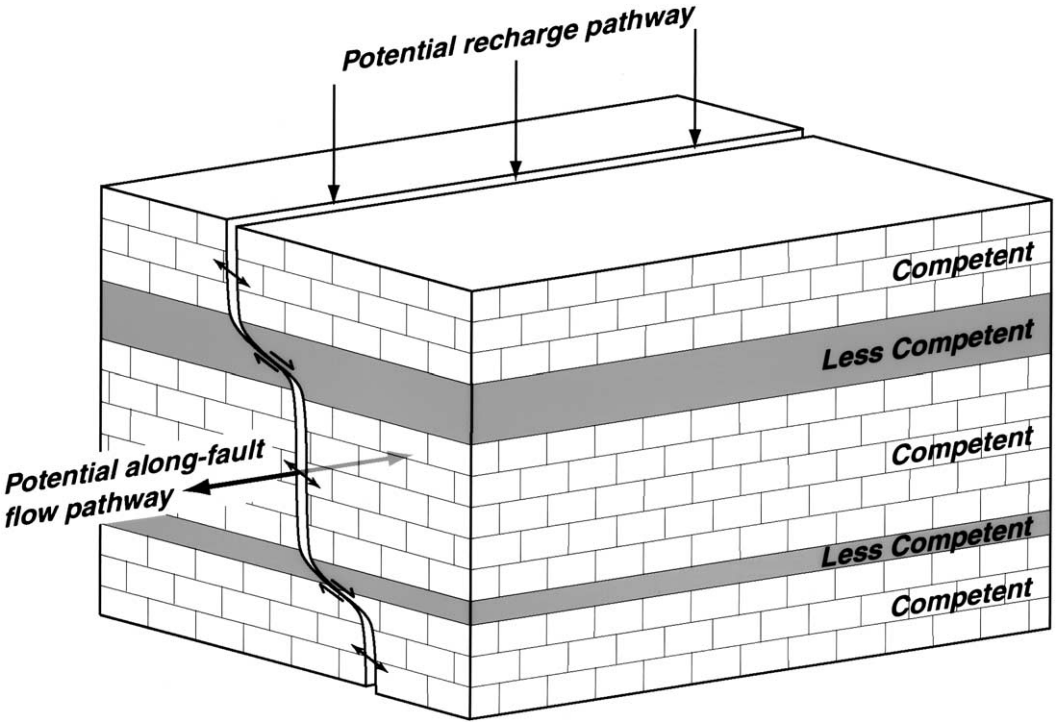

Fig. 8. Block diagram illustrating the role of dilational fault segments in shallow infiltration and subsurface groundwater flow.

steep fault segment. Whereas the overall cave geometry and position indicate lateral groundwater flow, a stalagmite visible on the cave floor attests to vertical movement of water along (and dripping from) the fault above the cave ceiling.

Dilational segments on small-displacement normal faults within the Edwards Aquifer are common sites of enhanced dissolution (Fig. 7a and b). Because faults can propagate through mechanically heterogeneous sequences, they tend to produce both vertically and laterally connected flow pathways (Fig. 8). Where these faults intersect the ground surface, they may be important pathways for shallow infiltration of groundwater as illustrated in Fig. 8. In the case of the Edwards Aquifer, the enhancement of flow pathways by dissolution may be accentuated by the weaker (lower fault dip) layers being more clay rich and therefore less permeable than the stronger (steeper fault dip) layers. The lower permeability of both the bed and fault segments in more clay-rich layers may inhibit downward flow, and lead to ponding of water within an overlying dilational fault segment. This is the reverse of the situation described by Dunham (1988) for ascending mineralizing fluids in the North Pennine Orefield (Section 4). Thus both structural (fault segment dilation) and lithologic influences may combine to increase potential for dissolution at interfaces between contrasting lithologies.

6. Conclusions

Rock failure in a mechanically layered sequence at shallow depths or high fluid pressures results in failure angles that vary with lithology. These variations in failure angle are caused by differences in friction angle or failure mode from layer to layer. Faults that cut several mechanical layers will have dip changes. The resulting refracted fault trajectories can therefore yield information about mechanical stratigraphy. Conversely, knowledge of mechanical stratigraphy and stress conditions at the time of failure can be used to make predictions of fault trajectories through a rock sequence. Refracted fault trajectories favor the development of dilational normal faults, which can develop in mechanically heterogeneous rock sequences by slip on faults cutting layers with different shear failure angles or different failure modes. Dilational normal faulting significantly enhances vertical infiltration and/or flow at the surface, and creates pathways for along-strike flow in the

Fig. 7. (a) and (b) Normal faults in the Kainer Formation of the Edwards Group Limestone exposed in the Balcones Fault Zone, along State Route 211, approximately 1 km south of San Geronimo, Texas (UTM zone 14; NAD 27; 521102 m E; 3275504 m N, 463 m elevation). Note that dissolution cavities are localized at steep, dilational segments of faults and are elongated parallel to fault strike. Lens cap (55 mm diameter) for scale. (a) Fault strike (right-hand rule) is 065–070. Dip values are indicated in white boxes. (b) Fault strike (right-hand rule) is 199–215. Dip values are indicated in white boxes. Layer A = bioturbated grainstone, packstone, and wackestone, Layer B = massive miliolid grainstone, and Layer C = massive (to bioturbated) miliolid grainstone and packstone.

subsurface. Recognition of the influence of mechanical stratigraphy on fault shape is an important component of the characterization of faulted aquifers, hydrocarbon reservoirs, and mineral provinces.

Acknowledgements

This work was funded by Southwest Research Institute through the SwRI Internal Research and Development Program (project #20.R9223.01.001). We thank Larry McKague and English Pearcy for helpful reviews, Stuart Birnbaum for conversations in the field, and Rebecca Emmot for preparation of the manuscript. We appreciate the editorial efforts of Tom Blenkinsop and reviews by David Peacock and Juan Watterson, which substantially improved the manuscript.

References

Anderson, J.E., Jr., Brown, J.B., Gries, J.C., Lovejoy, E.M.P., McKalips, D., Barnes, V.E., 1995. Geologic Atlas of Texas, Fort Stockton Sheet. The University of Texas at Austin Bureau of Economic Geology. Geologic Map and Accompanying Text, scale 1:250,000.

Barnes, V.E., 1976. Geologic Atlas of Texas, Pecos Sheet. The University of Texas at Austin Bureau of Economic Geology. Geologic Map and Accompanying Text, scale 1:250,000.

Childs, C., Nicol, A., Walsh, J.J., Watterson, J., 1996. Growth of vertically segmented normal faults. Journal of Structural Geology 18, 1389–1397.

Clark, A.K., 2000. Vulnerability of ground water to contamination, Edwards Aquifer recharge zone, Bexar County, Texas, 1998. U.S. Geological Survey Water-Resources Investigations Report 00-4149.

Collins, E.W., 2000. Geologic Map of the New Braunfels, Texas, 30 × 60 Minute Quadrangle: Geologic Framework of an Urban-Growth Corridor along the Edwards Aquifer, South-Central Texas. The University of Texas at Austin Bureau of Economic Geology, Miscellaneous Map No. 39.

Dunham, K.C., 1948. Geology of the Northern Pennine Orefield. Volume 1: Tyne to Stainmore. 1st edition. Memoirs of the Geological Survey of Britain.

Dunham, K.C., 1988. Pennine mineralization in depth. Proceedings of the Yorkshire Geological Society 47, 1–12.

Engelder, T., 1993. Stress Regimes in the Lithosphere. Princeton University Press, Princeton, NJ, USA.

Ferrill, D.A., Morris, A.P., Jones, S.M., Stamatakos, J.A., 1998. Extensional layer parallel shear and normal faulting. Journal of Structural Geology 20, 355–362.

Ferrill, D.A., Winterle, J., Wittmeyer, G., Sims, D.W., Colton, S., Armstrong, A., Morris, A.P., 1999. Stressed rock strains groundwater at Yucca Mountain, Nevada. GSA Today 9 (5), 1–8.

Ferrill, D.A., Morris, A.P., Sims, D.W., Stamatakos, J.A., 2000. Crossing conjugate normal faults. American Association of Petroleum Geologists Bulletin 84, 1543–1559.

Goodman, R.E., 1980. Introduction to Rock Mechanics. John Wiley and Sons, New York.

Groshong Jr, R.H., 1988. Low temperature deformation mechanisms and their interpretation. Geological Society of America Bulletin 100, 1329–1360.

Hancock, P.L., 1985. Brittle microtectonics: principles and practice. Journal of Structural Geology 7, 437–457.

Hoek, E., Brown, E.T., 1988. The Hoek–Brown failure criterion—a 1988 update. 15th Canadian Rock Mechanics Symposium, pp. 31–38.

Hovorka, S.D., Mace, R.E., Collins, E.W., 1998. Permeability structure of the Edwards Aquifer, South Texas—implications for aquifer management. The University of Texas, Bureau of Economic Geology Report of Investigations No. 250.

Maclay, R.W., Small, T.A., 1983. Hydrostratigraphic subdivisions and fault barriers of the Edwards Aquifer, south-central Texas, USA. Journal of Hydrology 61, 127–146.

Mandl, G., 1988. Mechanics of Tectonic Faulting. Elsevier, New York.

Mansfield, C.S., Cartwright, J.A., 1996. High resolution fault displacement mapping from three-dimensional seismic data: evidence for dip linkage during fault growth. Journal of Structural Geology 18, 249–263.

Morris, A.P., Ferrill, D.A., Henderson, D.B., 1996. Slip tendency analysis and fault reactivation. Geology 24, 275–278.

Peacock, D.C.P., Sanderson, D.J., 1992. Effects of layering and anisotropy on fault geometry. Journal of the Geological Society, London 149, 793–802.

Peacock, D.C.P., Zhang, X., 1994. Field examples and numerical modeling oversteps and bends along normal faults in cross-section. Tectonophysics 234, 147–167.

Sharp Jr, J.M., Banner, J.L., 1997. The Edwards Aquifer: a resource in conflict. GSA Today 7, 1–9.

Sibson, R.H., 1996. Structural permeability of fluid-driven fault-fracture meshes. Journal of Structural Geology 18, 1031–1042.

Stein, W.G., Ozuna. G.B., 1996. Geological framework and hydrogeologic characteristics of the Edwards Aquifer recharge zone, Bexar County, Texas. U.S. Geological Survey Water-Resources Investigations Report 95-4030: 8, and 1 plate, scale 1:75,000.

Wallace, W., 1861. The Laws which Regulate the Deposition of Lead Ores in Veins: Illustrated by Examination of the Geologic Structure of the Mining Districts of Alston Moor. Stanford, London.

Wilkins, S.J., Gross, M.R., 2002. Normal fault growth in layered rocks at Split Mountain, Utah: influence of mechanical stratigraphy on dip linkage, fault restriction and fault scaling. Journal of Structural Geology 24, 1413–1429.

Xiao, H., Suppe, J., 1989. Role of compaction in the listric shape of growth normal faults. American Association of Petroleum Geologists Bulletin 73, 777–786.

Zoback, M.L., Anderson, R.E., Thompson, G.A., 1981. Cainozoic evolution of the state of stress and style of tectonism of the basin and range province of the western United States. Philosophical Transactions of the Royal Society of London A300, 407–434.